

FULL PAPER

Fully relativistic study on electron impact elastic scattering from N^{q+} ($q = 1-3$), Na^+ , Ar^{q+} ($q = 1-3, 7-8$), and Xe^{q+} ($q = 2-6, 8$)

Dibyendu Mahato | Lalita Sharma | Rajesh Srivastava 

Department of Physics, Indian Institute of Technology, Roorkee, Uttarakhand, India

Correspondence

Rajesh Srivastava, Department of Physics, Indian Institute of Technology, Roorkee, Uttarakhand, India.
Email: rajesh.srivastava@ph.iitr.ac.in

Funding information

Science and Engineering Research Board, New Delhi, Govt. of India, Grant/Award Number: CRG/2020/005597.

Abstract

A study is presented on the elastic scattering of electrons from N^{q+} ($q = 1-3$), Na^+ , Ar^{q+} ($q = 1-3, 7-8$), Xe^{q+} ($q = 2-6, 8$) to understand the available experimental differential cross section results. A model potential approach has been utilized to describe the scattering process. The model potential includes the static, exchange, polarization and absorption potentials. The static potential is obtained through the charge density calculated by obtaining ionic wave functions using multi-configuration Dirac-Fock (MCDF) approximation. Thereafter, the static potential is added to the suitable exchange, polarisation and absorption potentials to construct the spherically averaged complex optical potential. Using the obtained potential in the Dirac equations, these are solved with the partial wave phase shift analysis method and the differential cross sections are calculated. Results for different ions exhibit prominent interference structures in the energy versus cross section curves and show good agreement on comparison with the experimental results available in the selected energy ranges.

KEYWORDS

elastic scattering, electron, ion, multi-configuration wave functions, relativistic

1 | INTRODUCTION

Study of electron-ion scattering and its cross sections are of fundamental interest as well as have importance in the semiconductor manufacturing processes, gas discharge lasers, and plasma diagnostics where electron collisions play an important role. Various possible processes in plasmas can be characterized by energy and angle dependent cross sections. In low-temperature plasmas (LTPs), the study on electron collisions with atoms, ions, molecules, and surfaces is very important for understanding and modeling LTPs [1]. Ion thrusters have become the propulsion choice due to over 90 percent fuel's efficiency. In particular, inert gases are being used as propellant in the modern ion thrusters, which eject high-speed ions so that there is no risk of the explosions associated with chemical propulsion. Since xenon is chemically inert, colorless, and odorless, it is of paramount significance for thrusters. Other inert gases, such as krypton and argon, also can be used [2] as propellant. Thus, the electron impact cross section studies on inert gas ions can be used as an input parameter in different simulation software to understand the plasma behavior as well as involved chemical and physical processes.

So far, only a few experimental and theoretical work have been reported on electron-ion elastic scattering above 10 eV. Therefore, it would be worth to first give a brief account of the experimental studies reported for some ions of our interest in this work. Huber et al. [3] performed the differential cross section (DCS) measurements using the crossed-beam experiment for Xe^{6+} and Xe^{8+} at incident electron energy of 50 eV in the angular range of $30^\circ-90^\circ$. Srigengan et al. [4] measured DCS with an electrostatic spectrometer for Na^+ at incident electron energy of 10 eV in the angular range of $25^\circ-95^\circ$. Srigengan et al. [5] reported experimental results on Ar^{2+} and Ar^{3+} at an incident electron energy of 16 eV.

Bélenger et al. [6] measured the DCS for Ar^{8+} and Xe^{q+} ($3 \leq q \leq 6$) at the scattering angles between 32° and 148° at low and intermediate energies. Williams et al. [7] measured the angular distributions of the electrons elastically scattered from N^{q+} ($q = 1 - 3$) at an energy 10 eV. McKenna and Williams [8] used a crossed-beam energy-loss spectrometer to measure the angular distribution for electron scattering from Ar^{2+} and Xe^{2+} ions at an incident electron energy 16 eV in between 20° and 60° angular range. Brotton et al. [9] reported the experimental DCS for Ar^+ ($3s^2 3p^2 2p$) in the angular range $35^\circ - 85^\circ$ with a similar technique as used by McKenna and Williams [8]. Wang et al. [10] measured the DCS for Ar^{8+} at 100 eV in the angular range from 34° to 85° using a 150° crossed beam experiment. Micheau et al. [11] performed the DCS measurements for Ar^+ at 16 eV between 100° and 180° scattering angles using a velocity-map imaging technique. However, on the theoretical side, there are few calculations performed on the elastic scattering of electrons from such ions. Huber et al. [3] performed DCS calculations using the Hartree-Fock method on Xe^{6+} and Xe^{8+} at the incident electron energy 50 eV. Srigengan et al. [4] calculated DCS for Na^+ ion at 10 eV using the phase-shift analysis method based on employing semi-empirical potential. Bélenger et al. [6] obtained the DCS for Ar^{8+} and Xe^{q+} ($3 \leq q \leq 6$) using the model potential technique with relativistic Hartree-Fock potential. Williams et al. [7] calculated the DCS for N^{q+} ($q = 1 - 3$) using semi-empirical potential at a single energy of 10 eV. McKenna and Williams [8] reported the DCS for Ar^{2+} and Xe^{2+} ions at an incident electron energy of 16 eV by solving Schrödinger equation with relativistic Hartree-Fock potential. These calculations were devoid of the polarization effects induced by the projectile electron. Shepherd and Dickinson [12] calculated the DCS for the elastic scattering of electron from Na^+ and N^{3+} at 10 eV as well as for Ar^{8+} at 12.98 and 22.46 eV, using model potential approach utilizing pseudopotential and quantum defect models. Brotton et al. [9] performed the DCS calculations for electron scattering from Ar^+ at collision energy of 16 eV by solving Hartree-Fock equations. Nishikawa et al. [13] calculated the DCS for Ar^{2+} and Ar^{7+} using the R-matrix method. Khandker et al. [14] obtained the DCS for Ar^+ to Ar^{18+} using Dirac relativistic partial wave analysis method, though by taking the neutral atom charge densities given by Koga [15], rather than taking correctly the ionic charge densities. From all these theoretical calculations, we find that there are different methods of varying accuracy which are mostly non-relativistic treatments which have been adopted to report the cross section results of the different ions. In our opinion, we need a consistent theoretical approach where such ions namely N^{q+} ($q = 1-3$), Na^+ , Ar^{q+} ($q = 1-3, 7-8$), and Xe^{q+} ($q = 2-6, 8$) should be studied using a fully relativistic approach, that is, both the projectile electron and target ions should be described separately through Dirac equations, because of the expected large spin-orbit and exchange effects. Therefore, in the present work, we have taken up the fully relativistic calculation of the elastic scattering of electron from such ions.

Electron interaction with the ions is mainly dominated by the strong attractive long-range Coulomb force between the two-point charges, that is, of projectile electron and residual ionic charge of target ion and further added with the short-range interaction between an incident electron and the target. It is observed that in the lower angular regions, the DCS show similar nature as obtained from Rutherford's formula but as the angular range increases the interference effect start showing structures in the cross sections. The static interaction between the electron and ion described the ion's electronic structure and is the most important part of the collision dynamics. This static interaction for electron-ion is different from a neutral atom by the strong attractive long-range Coulomb potential. In the present paper, we have used a multi-configuration Dirac-Fock (MCDF) approximation to calculate the ions' charge density. Thereafter, using the charge density, the static potential is calculated, which is further added with suitable exchange, polarization, and absorption potentials to construct the spherically averaged complex optical potential. Using the constructed potential in the Dirac equations, these are solved with the partial wave phase shift analysis method and the DCS are obtained.

In the next Section 2, we describe our method to evaluate the static potential from the calculated MCDF wave functions and the description of the optical model potential method used in the present work. In Section 3, we have discussed our obtained DCS results in detail for the various electron-ion scattering.

2 | THEORY

2.1 | Target ionic wave functions and charge density

The Dirac-Coulomb (DC) Hamiltonian of the N electron ionic system is expressed as [16].

$$H^{\text{DC}} = \sum_{i=1}^N (-i\alpha_i \cdot \nabla_i + \beta c^2 + V^N(r_i)) + \sum_{\substack{i < f \\ i, f=1}}^N \frac{1}{|r_i - r_f|}, \quad (1)$$

here, α and β are the standard Dirac matrices and $-i\nabla_i$ is the electron momentum operator. $V(r) = -\frac{Z}{r}$, is the central potential representing the electron-nucleus interaction. Further, using the MCDF method [16], the ionic bound state wave function ($\Phi^{\text{rel}}(\mathbf{1}, \mathbf{2}, \dots, \mathbf{N})$) can be expressed as a linear combination of various configurational state functions (CSFs) ($\Psi^{\text{rel}}(\mathbf{1}, \mathbf{2}, \dots, \mathbf{N})$), that is,

$$\Phi^{\text{rel}}(\mathbf{1}, \mathbf{2}, \dots, \mathbf{N}) = \sum_{i=1}^{N_{\text{CSF}}} a_i \Psi^{\text{rel}}(\mathbf{1}, \mathbf{2}, \dots, \mathbf{N}) \quad (2)$$

Here, N_{CSF} represents the total number of the CSFs utilized in the linear combination. Only those CSFs can be used in the combination that have the same total angular momentum and parity as of bound state wave function. a_i 's are the mixing coefficients which can be computed by diagonalizing the DC Hamiltonian. The required CSF can be expressed using Slater determinant in the form of one-electron Dirac spinor (ξ_{nkm}) as follows

$$\Psi^{\text{rel}}(\mathbf{1}, \mathbf{2}, \dots, \mathbf{N}) = \frac{1}{\sqrt{N!}} \{\xi_1(\mathbf{1})\xi_2(\mathbf{2})\dots\xi_N(\mathbf{N})\}, \quad (3)$$

where the Dirac spinor is,

$$\xi_{nkm}(\mathbf{r}, \sigma) = \frac{1}{r} \begin{pmatrix} P_{nk}(r)\chi_{km}(\hat{\mathbf{r}}, \sigma) \\ iQ_{nk}(r)\chi_{-km}(\hat{\mathbf{r}}, \sigma) \end{pmatrix}, \quad (4)$$

here, κ is the relativistic quantum number which is related to the orbital and total angular momentum as follows

$$\kappa = \begin{cases} l & \text{if } j = l - \frac{1}{2} \\ -(l+1) & \text{if } j = l + \frac{1}{2} \end{cases}. \quad (5)$$

In Equation (4), the P_{nk} and Q_{nk} are the large and small components of the radial wave functions, respectively, and satisfy the following orthogonality condition

$$\int_0^\infty dr [P_{n'\kappa}(r)P_{n\kappa}(r) + Q_{n'\kappa}(r)Q_{n\kappa}(r)] = \delta_{n'n}, \quad (6)$$

and the spinor spherical harmonics $\chi_{\pm km}$ is given by,

$$\chi_{km}(\hat{\mathbf{r}}, \sigma) = \sum_{\mu\nu} i\mu \frac{1}{2} \nu |jm\rangle Y_{l\mu}(\hat{\mathbf{r}}) \zeta_{\frac{1}{2}\nu}(\sigma), \quad (7)$$

and

$$\chi_{-km}(\hat{\mathbf{r}}, \sigma) = \sum_{\mu\nu} i\mu \frac{1}{2} \nu |jm\rangle Y_{l\mu}(\hat{\mathbf{r}}) \zeta_{\frac{1}{2}\nu}(\sigma). \quad (8)$$

here, $\bar{l} = 2j - 1$ and $(l_1 m_1 l_2 m_2 | jm)$ represents the Clebsch–Gordan coefficient. $Y_{l\mu}(\hat{\mathbf{r}})$ and $\zeta_{\frac{1}{2}\nu}(\sigma)$ are the spherical harmonics and spinor basis function, respectively. The spinor spherical harmonics satisfy the following ortho-normality condition

$$\langle \chi_{km}(\hat{\mathbf{r}}, \sigma) | \chi_{k'm'}(\hat{\mathbf{r}}, \sigma) \rangle = \delta_{k'\kappa} \delta_{m'm}. \quad (9)$$

Equations (6) and (9) collectively obey the following condition for the bound state orbitals, that is,

$$\langle \xi_i(\mathbf{r}, \sigma) | \xi_f(\mathbf{r}, \sigma) \rangle = \delta_{if}. \quad (10)$$

The large and small components of the radial wave functions corresponding to different ionic states are obtained using the GRASP2K [17] code under the MCDF approach.

The ground state electronic charge density $\rho(r)$ of the ion can be expressed by,

$$\rho(r) = \frac{1}{4\pi r^2} \sum_{\substack{i \in \text{all} \\ \text{subshells}}} \omega_i \left[p_{n_i k_i}^2(r_i) + Q_{n_i k_i}^2(r_i) \right]. \quad (11)$$

In the above equation, the ω_i is the occupation number for the i^{th} sub-shell and the electron in it is represented by the $n_i k_i$ quantum numbers.

2.2 | Optical model potential

The static potential is the spherically averaged distortion potential which is experienced by the incident projectile electron due to the ionic charged distributions of the target. In the present case, it is obtained by utilizing the ground state (i) potential of the target ion.

$$V_{\text{st}}(r_{N+1}) = -\frac{Z-N}{r_{N+1}} + \sum_{\substack{i \in \text{all} \\ \text{subshells}}} \omega_i \int_0^{\infty} \left[p_{n_i k_i}^2(r) + Q_{n_i k_i}^2(r) \right] \frac{1}{r_{>}} dr. \quad (12)$$

Here, r_{N+1} is the position coordinate of the projectile electron with respect to the nucleus of the target ion and $r_{>}$ is greater of r_{N+1} and r . The first term in the above equation is caused by the residual ionic charge $Z-N$, here as mentioned earlier Z is the atomic number of the target ion having N number of electrons. In the above expression of static potential, the first term thus represents the Coulomb potential while the second term is short-range potential.

With the static interaction $V_{\text{st}}(r)$, we have considered the indistinguishability of the projectile electron with the electrons in the target ion. To take account of this electron exchange effect in the present calculation, we have added the widely used exchange potential as given by Furness-McCarthy [18].

$$V_{\text{ex}} = \frac{1}{2} \{E - V_{\text{st}}(r)\} - \frac{1}{2} \left[\{E - V_{\text{st}}(r)\}^2 + 4\pi\rho(r) \right]^{1/2}. \quad (13)$$

where E is the incident electron energy. Further, to take polarization effect of the target ion by the projectile electron, we have included in a conventional manner, the Buckingham type polarization potential which affects the charges distribution of the target due to the projectile electron. When the projectile is far from the target, it can be expressed as,

$$V_{\text{pol}}(r) = -\frac{\alpha_d}{2r^4}, \quad (14)$$

where α_d is the dipole polarizability. We have taken only the asymptotic form of the polarization potential as for the electron-ion scattering, Coulomb potential is dominant and hence short-range correlation part of polarization is neglected.

Along with the elastic channel, we have also included the loss of incident electrons from the elastic channel to the inelastic channel by taking the semi-relativistic absorption potential given by Salvat [19, 20].

$$V_{\text{abs}} = \sqrt{\frac{2(E_L - m_e c^2)^2}{m_e c^2 (E_L - m_e c^2)}} \frac{\hbar}{2} A_{\text{abs}} [v_L \rho \sigma_{\text{bc}}(E_L, \rho, \Delta)]. \quad (15)$$

here local kinetic energy, $E_L = V_{\text{st}}(r) - V_{\text{ex}}(r)$ and the local velocity, $v_L = (2E/m_e)^{1/2}$. m_e represent electron rest mass, A_{abs} is an empirical parameter that takes the value of the order of unity, $\sigma_{\text{bc}}(E_L, \rho, \Delta)$ is the cross section for binary collisions of the projectile electron with the local free-electron gas calculated using non-relativistic Born approximation. Here Δ is the first excitation energy of the target ion under consideration.

Thus the total optical complex potential $V_{\text{opt}}(r)$ can be written as,

$$V_{\text{opt}}(r) = V_{\text{st}}(r) + V_{\text{ex}}(r) + V_{\text{pol}}(r) + iV_{\text{abs}}(r). \quad (16)$$

2.3 | Phase shifts and DCS

Further, we need to obtain the projectile electron wave function and the associated scattering phase shifts which relate to the scattering cross sections. For this purpose, we follow the conventional procedure for relativistic elastic scattering of electrons [19, 20], that is, the optical potential has been used in the Dirac equations and solved by using partial wave expansion method and adopting the following asymptotic ($r \rightarrow \infty$) boundary condition for the large component of the radial function, that is,

$$P_{E_k}(r) \sim \sin\left(kr - l\frac{\pi}{2} - \eta \ln 2kr + \delta_k\right). \quad (17)$$

where k is the relativistic momentum wave number of the projectile electron, l is the number of the partial waves, and η is the Sommerfeld parameter, that is,

$$\eta = \frac{Ze^2 m_e}{\hbar k}. \quad (18)$$

In Equation (17) δ_k is the total phase shift which is the sum of the phase shifts due to the short-range potential ($\hat{\delta}_k$) and Coulomb phase shift (Δ_k) at $Z = Z_\infty$ (the residual ionic charge of the target). To find the short range phase shift ($\hat{\delta}_k$), the radial equations are integrated from $r = 0$ to a certain distance r_m beyond which $r > r_m$, the field is purely Coulombian, thus the large component radial Dirac function can be expressed as

$$P_{E_k}(r) = \cos \hat{\delta}_k f_{E_k}^{(u)}(r) + \sin \hat{\delta}_k g_{E_k}^{(u)}(r), \quad (19)$$

where $f_{E_k}^{(u)}(r)$ and $g_{E_k}^{(u)}(r)$ are the regular and irregular Dirac functions for $Z = Z_\infty$. Thus the short range phase shift $\hat{\delta}_k$ is determined by matching the outer and inner solution at r_m , with the continuity of the radial function $P_{E_k}(r)$ and its derivatives as

$$\exp(2i\hat{\delta}_k) = \frac{D_{\text{out}}[f_{E_k}^{(u)}(r_m) + g_{E_k}^{(u)}(r_m)] - \left[\left(f_{E_k}^{(u)}\right)'(r_m) + \left(g_{E_k}^{(u)}\right)'(r_m)\right]}{\left[\left(f_{E_k}^{(u)}\right)'(r_m) + \left(g_{E_k}^{(u)}\right)'(r_m)\right] - D_{\text{out}}[f_{E_k}^{(u)}(r_m) + g_{E_k}^{(u)}(r_m)]}. \quad (20)$$

where the prime indicates the derivatives with respect to r and D_{out} is the logarithmic derivatives of the outgoing numerical radial function at the matching point. The phase shift for the Coulomb potential (Δ_k) is given by

$$\Delta_k = \arg[\zeta(E + 2m_e c^2) - i(\kappa + \lambda)ch\kappa] - (\lambda - l - 1)\frac{\pi}{2} + \arg\Gamma(\lambda + i\eta) - S(\zeta, \kappa)\pi, \quad (21)$$

where $\zeta = Z/137$, $\lambda = \sqrt{\kappa^2 - \zeta^2}$ and $S(\zeta, \kappa) = 1$ if $\zeta < 0$ and $\kappa < 0$, and zero otherwise.

Thus in the presence of Coulomb and short range potentials, the direct and spin-flip scattering amplitudes can be expressed as,

$$f(\theta) = f_{\text{sr}}(\theta) + f^{(C)}(\theta) \text{ and } g(\theta) = g_{\text{sr}}(\theta) + g^{(C)}(\theta). \quad (22)$$

where $f_{\text{sr}}(\theta)$ and $g_{\text{sr}}(\theta)$ are the scattering amplitude contributions due to the short-range part of the potential given below as

$$f_{\text{sr}}(\theta) = \frac{1}{2ik} \sum_{l=0}^{\infty} \{ (l+1) \exp(2i\Delta_{-l-1}) [\exp(2i\hat{\delta}_{-l-1}) - 1] + l \exp(2i\Delta_l) [\exp(2i\hat{\delta}_l) - 1] \} P_l(\cos \theta), \quad (23)$$

and

$$g_{\text{sr}}(\theta) = \frac{1}{2ik} \sum_{l=0}^{\infty} \{ \exp(2i\Delta_l) [\exp(2i\hat{\delta}_l) - 1] - \exp(2i\Delta_{-l-1}) [\exp(2i\hat{\delta}_{-l-1}) - 1] \} P_l^1(\cos \theta). \quad (24)$$

Also, the scattering amplitude contribution for the Coulomb interaction with $Z = Z_\infty$, $f^{(C)}(\theta)$ and $g^{(C)}(\theta)$ can be expressed as

$$f^{(C)}(\theta) = \frac{1}{2ik} \sum_{l=0}^{\infty} \{ (l+1) [\exp(2i\Delta_{-l-1}) - 1] + l [\exp(2i\Delta_l) - 1] \} P_l(\cos \theta), \quad (25)$$

and

$$g^{(C)}(\theta) = \frac{1}{2ik} \sum_{l=0}^{\infty} \{ \exp(2i\Delta_l) - \exp(2i\Delta_{-l-1}) \} P_l^1(\cos \theta). \quad (26)$$

Further using Equation (22), we can calculate the required DCS as

$$\frac{d\sigma}{d\Omega} = |f(\theta)|^2 + |g(\theta)|^2. \quad (27)$$

3 | RESULTS AND DISCUSSIONS

We have first calculated the ground state MCDF wave functions of the various ionic targets N^{q+} ($q = 1-3$), Na^+ , Ar^{q+} ($q = 1-3, 7-8$), and Xe^{q+} ($q = 2-6, 8$) considered in the present work. The calculated wave functions have been used to obtain their ionic charge densities. Thereafter, the optical model potential for each ion is obtained. Using the charge density (Equation 11), the static potential (Equation 12) is calculated, which is further added with suitable exchange (Equation 13), polarization (Equation 14), and absorption (Equation 15) potentials to construct the spherically averaged complex optical potential (Equation 16). Thereafter, the relativistic Dirac equations are solved using this optical potential and the partial wave analysis approach. The phase shifts are obtained with which the DCS results of the different ions calculated.

3.1 | Calculation of Dirac-Fock wave functions of the ionic targets

For an accurate description of the ground state of the ions considered in the present calculation, we have obtained the MCDF wave functions from the GRASP2k [17] program. In the MCDF approach as mentioned earlier, any atomic state function is written as a linear combination of the configuration state functions with the same total angular momentum and parity of the target ion. The term symbol for the respective ground states, their representation in the MCDF framework and the mixing coefficients are given in Table 1. We have included here only those fine structure states whose contribution to the ground state are as small as 0.001.

The dipole polarizability α_d of the target ions required in the polarization potential (Equation 14) are given in Table 2, which are taken from References [21–26].

Further, the first excitation energy Δ of the target ions required in the absorption potential (Equation 15) are given in Table 3 and these are taken from References [27–30].

3.2 | DCS results

Since experimental DCS results for different ions are available for comparison at few selected incident electron energies, we have performed our calculations only at those energies. Most of these experimental cross sections are relative measurements, therefore, we have normalized them with our calculated DCS at an angle where our results give the overall best agreement with the experiment. In fact, we observed that for the electron-ion scattering, the DCS results do not show the structures and fall off monotonically following the Rutherford scattering formula and also where all the theoretical calculations give almost same results. It is only in the intermediate and higher scattering angles the structures in the cross section curves show up and the magnitudes of the DCS from different theories differ. For the sake of experimental data normalization and comparison purposes, we have also carried out the calculations for all the ions using the Rutherford scattering formula.

In Figure 1A–C, we have shown at 10 eV incident electron energy, the DCS results for the three N^{q+} ($q = 1-3$) ions respectively and compared our results with the available measurements and theoretical calculations of Williams et al. [7] in the scattering angle range of $30^\circ-60^\circ$. Their calculation is based on using single semi-empirical potential, that is, independent particle model potential of Green et al. [31] in the Schrodinger equation and adopting phase shift analysis by taking only few partial waves. We also compared with the theoretical calculations of Shepherd and Dickinson [12] available for N^{3+} ion only, where they also used some sort of different independent particle model potential similar to Williams

TABLE 1 Term symbols and mixing coefficients for the MCDF wavefunctions of the ionic ground states

Ion	Term symbol	Ground state wavefunction and mixing coefficients
N^+	3P_0	$a_1 2\bar{p}^2 + a_2 2\bar{p}3\bar{p} + a_3 2p^2 + a_4 2p3p + a_5 3s^2 + a_6 3\bar{p}^2 + a_7 3p^2$ $a_1 = 0.81237, a_2 = -0.09917, a_3 = -0.57039, a_4 = 0.06923, a_5 = 0.00003, a_6 = -0.00661, a_7 = 0.00461$
	$2\text{P}_{1/2}$	$a_1 2\bar{p} + a_2 3\bar{p}$ $a_1 = 0.99990, a_2 = -0.00058$
N^{2+}	1S_0	$a_1 2s^2 + a_2 2s3s + a_3 2\bar{p}^2 + a_4 2p^2 + a_5 3s^2$ $a_1 = 0.96992, a_2 = -0.02282, a_3 = 0.00001, a_4 = 0.24536, a_5 = 0.00833$
	1S_0	$2\bar{p}^2 2p^4 + a_2 2\bar{p}^2 2p^3 3p + a_3 2\bar{p}^2 2p^2 3s^2 + a_4 2p2p^4 3\bar{p} + a_5 2p^4 3s^2$ $a_1 = 0.977945, a_2 = -0.16490, a_3 = 0.00542, a_4 = -0.11592, a_5 = 0.00380$
Ar^+	$2\text{P}_{3/2}$	$a_1 3\bar{p}^2 3p^3 + a_2 3\bar{p}^2 3p^2 4\bar{p} + a_3 3\bar{p}^2 3p^2 4p + a_4 3\bar{p}^2 3p^2 4s^2 + a_5 3\bar{p}^2 3p^2 4\bar{p} + a_6 3\bar{p}^2 3p^2 4p + a_7 3\bar{p}^2 3p^2 4\bar{p} + a_8 3\bar{p}^2 3p^2 4s^2 + a_9 3\bar{p}^2 3p^2 4p + a_{10} 3\bar{p}^2 3p^2 4\bar{p} + a_{11} 3\bar{p}^2 3p^2 4s^2 + a_{12} 3\bar{p}^2 3p^2 4p$ $a_1 = 0.99279, a_2 = 0.00022, a_3 = -0.03550, a_4 = 0.11226, a_5 = 0.00599, a_6 = 0.00201, a_7 = 0.00228, a_8 = -0.00060, a_9 = 0.01457, a_{10} = 0.00008, a_{11} = 0.01450, a_{12} = 0.00509$
	$2\text{P}_{1/2}$	$a_1 3\bar{p}^2 3p^2 4\bar{p} + a_2 3\bar{p}^2 3p^2 4p + a_3 3\bar{p}^2 3p^2 4s^2 + a_4 3\bar{p}^2 3p^2 4\bar{p} + a_5 3\bar{p}^2 3p^2 4p + a_6 3\bar{p}^2 3p^2 4s^2 + a_7 3\bar{p}^2 3p^2 4\bar{p} + a_8 3\bar{p}^2 3p^2 4p$ $a_1 = 0.00047, a_2 = -0.01411, a_3 = 0.99040, a_4 = -0.00001, a_5 = 0.0936, a_6 = -0.09990, a_7 = 0.00825, a_8 = -0.00194$
Ar^{2+}	3P_2	$a_1 3\bar{p}^2 3p^2 + a_2 3\bar{p}^2 3p4\bar{p} + a_3 3\bar{p}^2 3p4p + a_4 3\bar{p}^2 3p^3 + a_5 3\bar{p}^2 3p^2 4\bar{p} + a_6 3\bar{p}^2 3p^2 4p + a_7 3\bar{p}^2 3p^2 4\bar{p} + a_8 3\bar{p}^2 3p^2 4p + a_9 3\bar{p}^2 3p^2 4\bar{p} + a_{10} 3\bar{p}^2 3p^2 4p + a_{11} 3\bar{p}^2 3p^2 4\bar{p}$ $a_1 = 0.83724, a_2 = -0.01198, a_3 = -0.05589, a_4 = 0.53710, a_5 = -0.04781, a_6 = -0.01219, a_7 = -0.04171, a_8 = -0.02899, a_9 = 0.03438, a_{10} = 0.02899, a_{11} = 0.01599$
	$4\text{S}_{3/2}$	$a_1 3\bar{p}^2 3p + a_2 3\bar{p}^2 4p + a_3 3\bar{p}^2 3p^2 + a_4 3\bar{p}^2 3p4\bar{p} + a_5 3\bar{p}^2 3p4p + a_6 3\bar{p}^2 3p4\bar{p} + a_7 3\bar{p}^2 3p4p + a_8 3\bar{p}^2 3p4\bar{p} + a_9 3\bar{p}^2 3p4p + a_{10} 3\bar{p}^2 3p4\bar{p} + a_{11} 3\bar{p}^2 3p4p$ $a_1 = 0.49139, a_2 = -0.07323, a_3 = 0.07427, a_4 = 0.01525, a_5 = 0.01949, a_6 = -0.03149, a_7 = -0.01799, a_8 = -0.45100, a_9 = 0.02571, a_{10} = 0.01113, a_{11} = -0.02379$
Ar^{7+}	$2\text{S}_{1/2}$	$a_1 3s + a_2 4s$ $a_1 = 1.00000, a_2 = -0.00097$
	1S_0	$a_1 2\bar{p}^2 2p^4 + a_2 2\bar{p}^2 2p^3 3p + a_3 2\bar{p}^2 2p^3 4p + a_4 2\bar{p}^2 2p^4 3\bar{p} + a_5 2\bar{p}^2 2p^4 4p$ $a_1 = 0.99704, a_2 = -0.05698, a_3 = -0.02663, a_4 = -0.04103, a_5 = -0.01624$
Xe^{2+}	3P_2	$a_1 5\bar{p}^2 5p^2 + a_2 5\bar{p}^2 5p5\bar{p} + a_3 5\bar{p}^2 5p6p + a_4 5\bar{p}^2 5p^3 + a_5 5\bar{p}^2 5p^2 6\bar{p} + a_6 5\bar{p}^2 5p^2 6p + a_7 5\bar{p}^2 5p^2 6\bar{p} + a_8 5\bar{p}^2 5p^2 6p + a_9 5\bar{p}^2 5p^2 6\bar{p} + a_{10} 5\bar{p}^2 5p^2 6p + a_{11} 5\bar{p}^2 5p^2 6\bar{p}$ $a_1 = 0.94623, a_2 = -0.00891, a_3 = -0.059532, a_4 = 0.30998, a_5 = -0.04588, a_6 = -0.04269, a_7 = -0.00370, a_8 = -0.01896, a_9 = 0.01297, a_{10} = 0.01396, a_{11} = 0.01628$
	$4\text{S}_{3/2}$	$a_1 5\bar{p}^2 5p + a_2 5\bar{p}^2 6p + a_3 5\bar{p}^2 5p^2 + a_4 5\bar{p}^2 5p6\bar{p} + a_5 5\bar{p}^2 5p6p + a_6 5\bar{p}^2 5p6\bar{p} + a_7 5\bar{p}^2 5p6p + a_8 5\bar{p}^2 5p6\bar{p} + a_9 5\bar{p}^2 5p6p + a_{10} 5\bar{p}^2 5p6\bar{p} + a_{11} 5\bar{p}^2 5p6p$ $a_1 = 0.70731, a_2 = -0.02521, a_3 = 0.62824, a_4 = 0.02358, a_5 = 0.02800, a_6 = -0.02077, a_7 = -0.01126, a_8 = -0.31941, a_9 = 0.01843, a_{10} = 0.00841, a_{11} = -0.00704$
Xe^{4+}	3P_0	$a_1 5\bar{p}^2 + a_2 5p6\bar{p} + a_3 5p^2 + a_4 5p6p$ $a_1 = 0.96980, a_2 = -0.02763, a_3 = -0.24240, a_4 = 0.00022$
	$2\text{P}_{1/2}$	$a_1 5\bar{p} + a_2 6\bar{p}$ $a_1 = 0.99995, a_2 = -0.00948$
Xe^{6+}	1S_0	$a_1 5s^2 + a_2 5p^2 + a_3 5p^2$ $a_1 = 0.99340, a_2 = 0.00149, a_3 = -0.11472$
	1S_0	$a_1 4d^4 4d^4 + a_2 4d^4 4d^5 5d + a_3 4d^3 4d^5 5d$ $a_1 = 0.99704, a_2 = -0.05698, a_3 = -0.02663, a_4 = -0.04103, a_5 = -0.01624$

TABLE 2 Polarizabilities of ions in Å³

Ion	Polarizability (Å ³)	Ion	Excitation energy (Å ³)
N ⁺	0.5448	Ar ²⁺	1.0362
N ³⁺	0.3553	Ar ³⁺	0.5773
Na ⁺	0.2546	Ar ⁸⁺	0.0046
Ar ⁺	1.0658	Xe ⁸⁺	0.2190

TABLE 3 Excitation energies of ions in eV

Ion	Excitation energy (eV)	Ion	Excitation energy (eV)	Ion	Excitation energy (eV)
N ⁺	11.20	Ar ²⁺	14.19	Xe ³⁺	13.52
N ²⁺	11.70	Ar ³⁺	16.29	Xe ⁴⁺	13.58
N ³⁺	10.31	Ar ⁷⁺	17.59	Xe ⁵⁺	14.17
Na ⁺	32.89	Ar ⁸⁺	251.26	Xe ⁶⁺	14.42
Ar ⁺	13.42	Xe ²⁺	13.16	Xe ⁸⁺	57.26

et al. [7]. We observe from these Figure 1A–C that for all the three N^{q+} ($q = 1 - 3$) ions, our results, agree very well with the DCS measurements and theoretical calculations of Williams et al. [7] available only in the angular range of 30°–60°. Beyond this angular region, we find that our cross section curves from the three different ions show minima in the range 100°–120° while the curves from the Rutherford formula do not show any structure but fall off smoothly in the close vicinity of other curves. This difference of non-occurrence of minimum as seen in the results from Rutherford formula exhibits the role or contributions of the additional effect of short-range potential and inclusion of relativistic effects in our calculations over the long-range of Coulomb potential. An excellent agreement of our results has been noticed for N³⁺ with the calculation of Shepherd and Dickinson [12] for the entire scattering angles except at the minimum position, which might be due to difference in our method with theirs.

In Figure 2, we have shown our DCS results for the scattering of electrons from Na⁺ ion at 10 eV incident electron energy. In fact, Srigenan et al. [4] reported their DCS measurements for Na⁺ only at 10 eV incident electron energy in the range of 30°–100° scattering angles. In order to compare with their DCS results, we have carried out our calculations and these are shown and compared with their results in Figure 2. In the angular range 30°–100° where measured data are reported, we observe that our calculations are in excellent agreement with the experimental results of Srigenan et al. [4] and predict the similar angular variation of the cross sections, that is, showing first minimum between 40° and 65° angular range and next maximum between 80° and 100°. In the present calculation, we observe a second minimum around 120°–140° which also seems to follow the behavior anticipated from the experimental data of Srigenan et al. [4]. The calculations of Shepherd and Dickinson [11] also show good agreement with our results up to 135°, then their results show slightly lower cross sections. As expected the results from Rutherford formula show good agreement with experiment and theoretical calculations only up to 40° scattering angles and thereafter fall off with average magnitude without showing any structures in the cross section curve. This feature can again be explained on the basis that Na⁺ cannot be considered as point charge and has effects of its electronic structure giving rise to short range potentials and possibly the contribution coming from relativistic spin-orbit and exchange effects as well.

In Figure 3A–F, we have compared our calculated DCS results for multiply charged argon ions [Ar^{q+} ($q = 1-3, 7-8$)] with the measurements of Srigenan et al. [5], Bélenger et al. [6], McKenna and Williams [8], Brotton et al. [9], Wang et al. [10], and Micheau et al. [11] as well as with the theoretical calculations of Srigenan et al. [5], Bélenger et al. [6], McKenna and Williams [8], Brotton et al. [9], Shepherd and Dickinson [12], and Khandker et al. [14]. We first compare our electron scattering cross section results for Ar⁺ in Figure 3A. As Ar⁺ ion has (3s²3p²2p) configuration which can give rise to two fine-structure levels, that is, $J = 1/2$ and $J = 3/2$, we have taken the average sum of the cross sections of both the levels of the ground state configurations by using appropriate weighting factors. In Figure 3A, we have compared our calculated DCS results for Ar⁺ at 16 eV incident electron energy with the available measurements of Brotton et al. [9] in the range of 30°–90° scattering angles as well as with their theoretical results in the overlapping angular range. Comparisons are also made with the experimental data of Micheau et al. [11] in the angular range of 100°–180° as well as with the theoretical calculations of Khandker et al. [14].

We find excellent agreement of our calculations with the theoretical and experimental results of Brotton et al. [9] along with the occurrence of a similar minimum around 80°. In fact, the calculation of Brotton et al. [9] are somewhat similar to ours which is fully relativistic but theirs is a semi-relativistic type where they have described the scattering problem by solving Hartree–Fock equations and included spin-orbit coupling effect empirically. In the backscattering angles, our results also show overall good agreement with the experimental data of Micheau et al. [11] but with a presence a deeper minimum around 142° as compared with the measurements. On comparison of our results for Ar⁺ with the available other theoretical calculation, that is, of Khandker et al. [14], we find the agreement is good but their calculation slightly overestimates the DCS

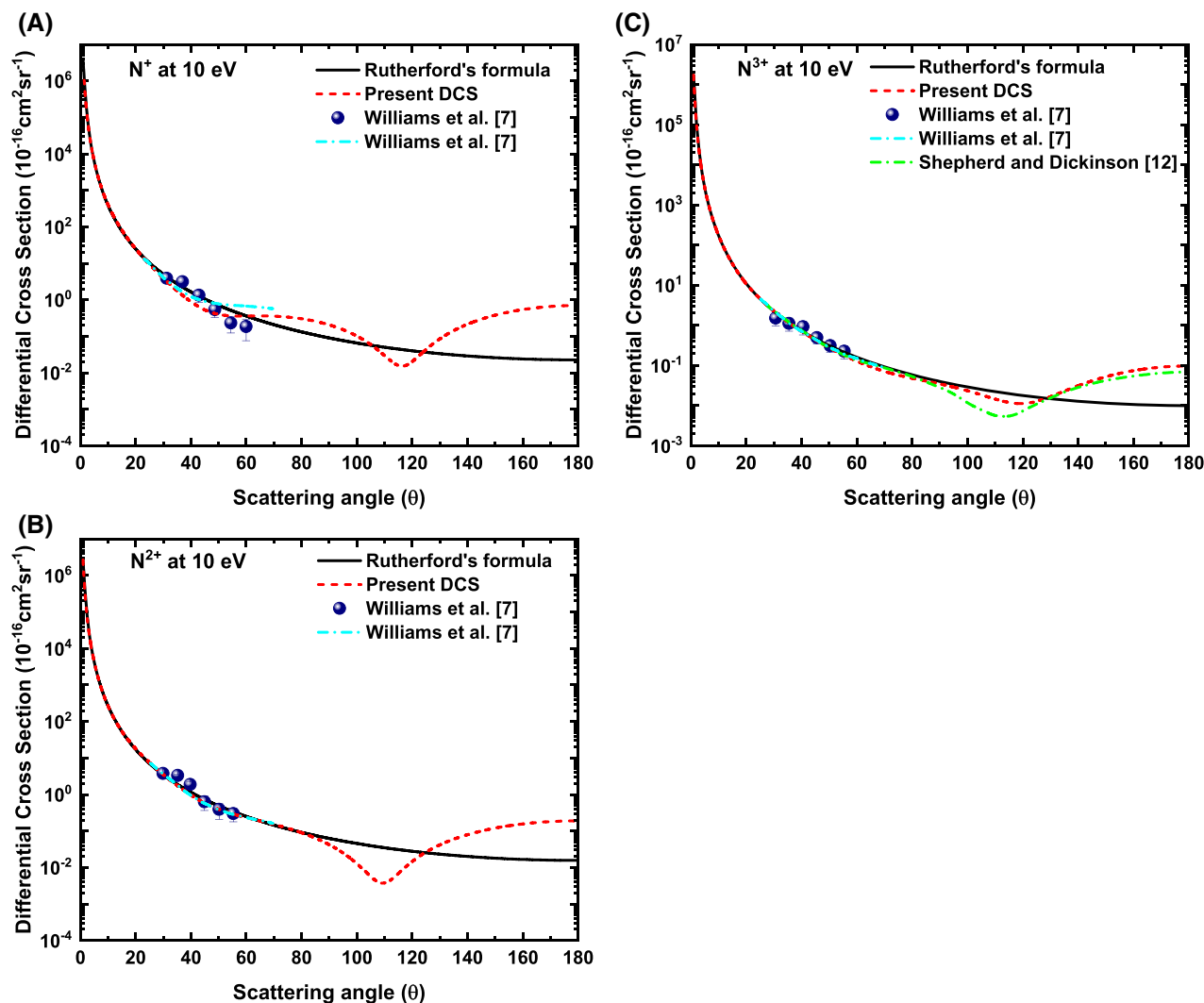


FIGURE 1 Electron impact differential cross sections at 10 eV incident electron energy for (A) N^+ , (B) N^{2+} , and (C) N^{3+}

values in the forward scattering angles and thereafter underestimates in the backward scattering angles. In actual fact, Khandker et al. [14] in their paper reported the results of the DCS for electron scattering from many multi-charged Ar ions. The difference in their calculation with ours is due to some important factors, for example, though they described the electron– Ar^{q+} scattering through Dirac equations by using ELESIPA code [20] but they used available Hartree–Fock analytical electron density of neutral Ar atom given by Koga [15] and the neutral Ar atomic dipole polarizability for their calculation (as available in the ELESIPA code). In fact, such choice of Khandker et al. [14] to describe the electron– Ar^{q+} collisions is somewhat inconsistent and not reliable. Further, the results from Rutherford formula show usual behavior as seen and explained in the previous figures for the DCS of scattering from N and Na ions. Further, in Figure 3B, our results for Ar^{2+} at 16 eV incident electron energy are shown and compared with the measurements of Srigengan et al. [5] and McKenna and Williams [8] as well as theoretical results of McKenna and Williams [8] and Khandker et al. [14]. We observe from this Figure 3B that present DCS results are in good agreement with the measurements of Srigengan et al. [5] and McKenna and Williams [8] and show a similar minimum around scattering angle of 82° . Also similar is the agreement with other calculations in the scattering angular region up to 80° . We also observe our cross section curve shows second minimum at 145° , whereas Khandker et al. [14] get this minimum around 139° . Again the differences in the results of Khandker et al. [14] and ours are due to the same reason as discussed in respect to the Figure 3A for electron– Ar^+ scattering. In Figure 3C, we have shown the DCS results for electron scattering from Ar^{3+} at 16 eV and compared with the available measurement of Srigengan et al. [5] and notice a reasonable agreement. Further, we see that our calculations show good agreement with the theoretical results of Srigengan et al. [5], whereas the results of Khandker et al. [14] are slightly different and show minima at different angular positions. We would like to add here that the position of minimum in the cross section curves, in the forward scattering angles is very much dependent on the polarization potential or on the value of the ionic dipole polarizability. So, for accurate DCS calculation, we must use the reliable dipole polarizability of the ions in order to get good agreement with the experiment. As pointed out earlier that our values of the dipole polarizability of ions which we have chosen accurately are given in Table 2 and we can say that our such a choice has

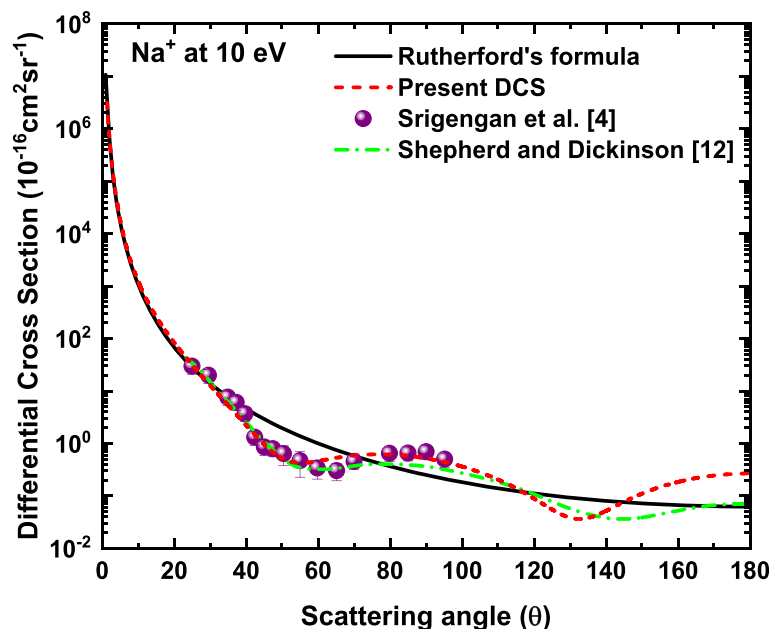


FIGURE 2 Electron impact differential cross sections for Na^+ at 10 eV

reflected in the good comparison of our cross sections with the experimental results. In Figure 3D, our present DCS results for Ar^{7+} at 100 eV are shown and compared with the measurements of Wang et al. [10] available in the angular range of 30° – 90° as well as the theoretical calculations of Nishikawa et al. [13] and Khandker et al. [14]. We observe that all the theoretical calculations including the results from Rutherford formula and experimental values are in complete agreement in the forward scattering angles up to nearly 90° . At such a high incident electron energy of 100 eV, the effect of short range potential becomes less effective, thus, it is quite expected that only Coulomb potential will dominate for highly charged Ar^{7+} ion and as a result all the theoretical curves should almost merge, thus we get a similar nature of curves as obtained by Nishikawa et al. [13] and Khandker et al. [14]. In Figure 3E,F, we have shown our results for highly charged Ar^{8+} at incident electron energies of 12.98 and 22.46 eV respectively and compared these with the experimental and theoretical results of Bélenger et al. [6] and the calculations of Shepherd and Dickinson [12] and Khandker et al. [14]. Since Ar^{8+} is highly charged ion and the incident electron will realize huge Coulomb potential which will dominate over the short range static and exchange potentials even though both the incident energies are not so high. Consequently, from Figure 3E,F, we observe perfect agreement of our and other theoretical calculations [5, 11, 13] up to 120° with the experimental results of Bélenger et al. [6]. Thereafter except the results from Rutherford formula rest curves show second minimum around 128° – 135° which is though not supported by the theoretical and experimental results of Bélenger et al. [6]. It should be noted that the theoretical calculation of Bélenger et al. [6] is of semi-relativistic type and uses the relativistic Hartree–Fock potential and does not include the polarization potential in their calculation and hence no dip or minimum is seen in their results which is artifact of polarization effect.

We have calculated and shown in the Figures 4 and 5, the DCS for some six xenon ions (Xe^{q+} ($q = 2$ – 6 , 8)) at selected incident electron energies for which experimental results are available for comparison. Thus, we compared our results with the measurements of Huber et al. [3], Bélenger et al. [6] and McKenna and Williams [8] and calculations of Bélenger et al., [6] and McKenna and Williams [8]. For some of the xenon ions, we found, their values of dipole polarizability were not available and hence to avoid error in the calculation, we dropped the polarization potential for them in the optical potential and used only static, exchange and absorption potentials to find out the DCS. Before we compare our calculations with other available results, it is important to mention in the beginning itself that our present results show several maxima and minima, which is quite expected as xenon is a high atomic number $Z = 54$ element and its neutral or ionic wave functions have many nodes and thus give rise to oscillatory short range potential which make the DCS to oscillate. This is in contrast to the results from Rutherford formula which show no structures in the DCS curve. In Figure 4A, we have plotted the DCS results for Xe^{2+} at 16 eV and compared with the measurement of McKenna and Williams [8] available in the forward angles. Our DCS show two minima one around 55° and the other near 98° which seem to match very well with the measurement of McKenna and Williams [8]. There is another minimum noticed in the present calculation around 139° but there are no experimental results to compare and confirm it. Our result for Xe^{3+} at 43.07 eV are shown in Figure 4B and these are compared with the theoretical and experimental results of Bélenger et al. [6]. In the range where experimental results are available up to 40° , all the three results agree completely. Whereas, the theoretical result of Bélenger et al. [6] shows slightly higher cross sections but get similar minimum around 145° , the same as seen in the present calculated results. In Figure 4C,D respectively, our DCS results for Xe^{4+} at 43.83 eV and Xe^{5+} at 43.10 eV are again compared with the measurement and

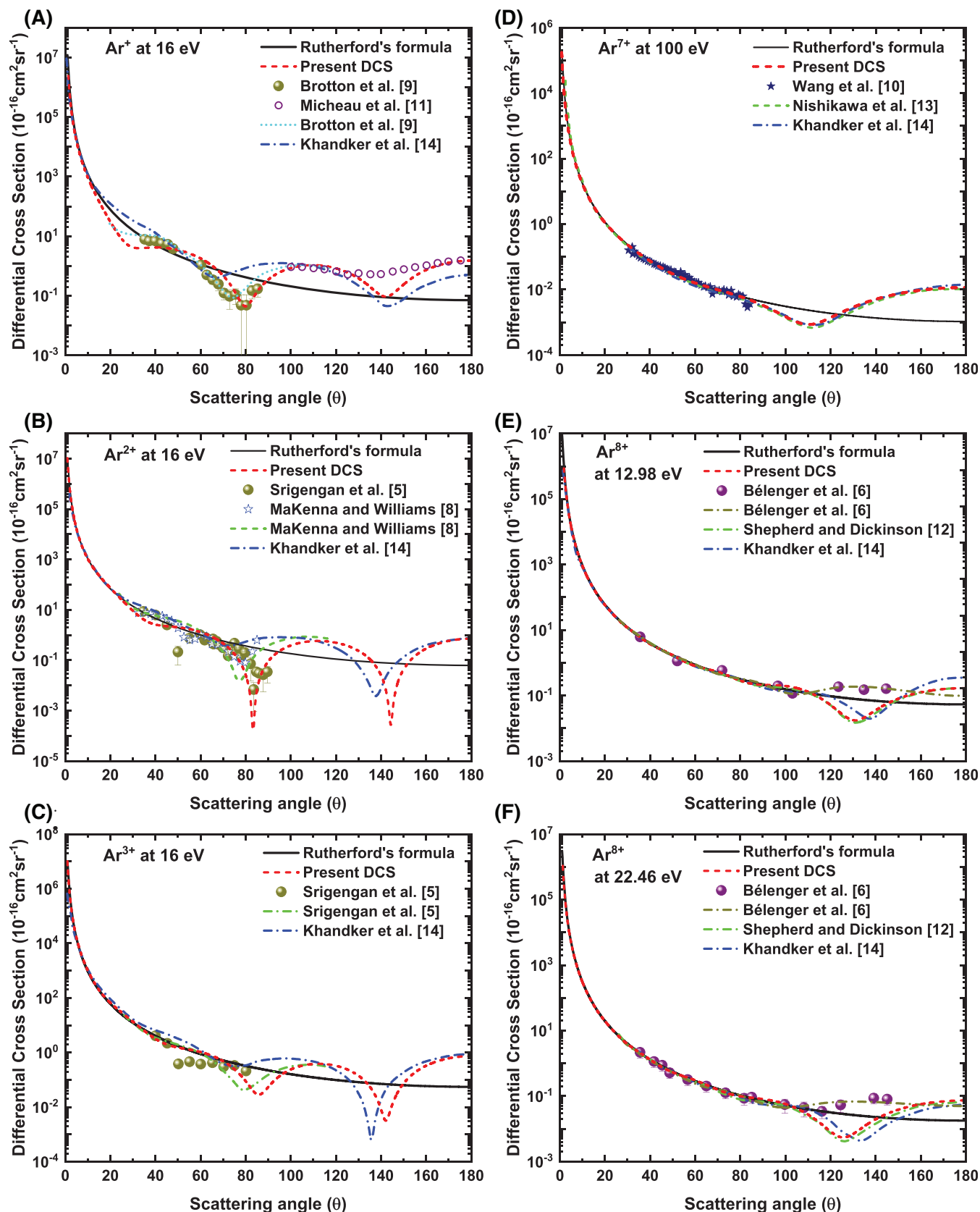


FIGURE 3 Electron impact differential cross sections for (A) Ar^+ at 16 eV, (B) Ar^{2+} at 16 eV, (C) Ar^{3+} at 16 eV, (D) Ar^{7+} at 100 eV, (E) Ar^{8+} at 12.98 eV, and (F) Ar^{8+} at 22.46 eV

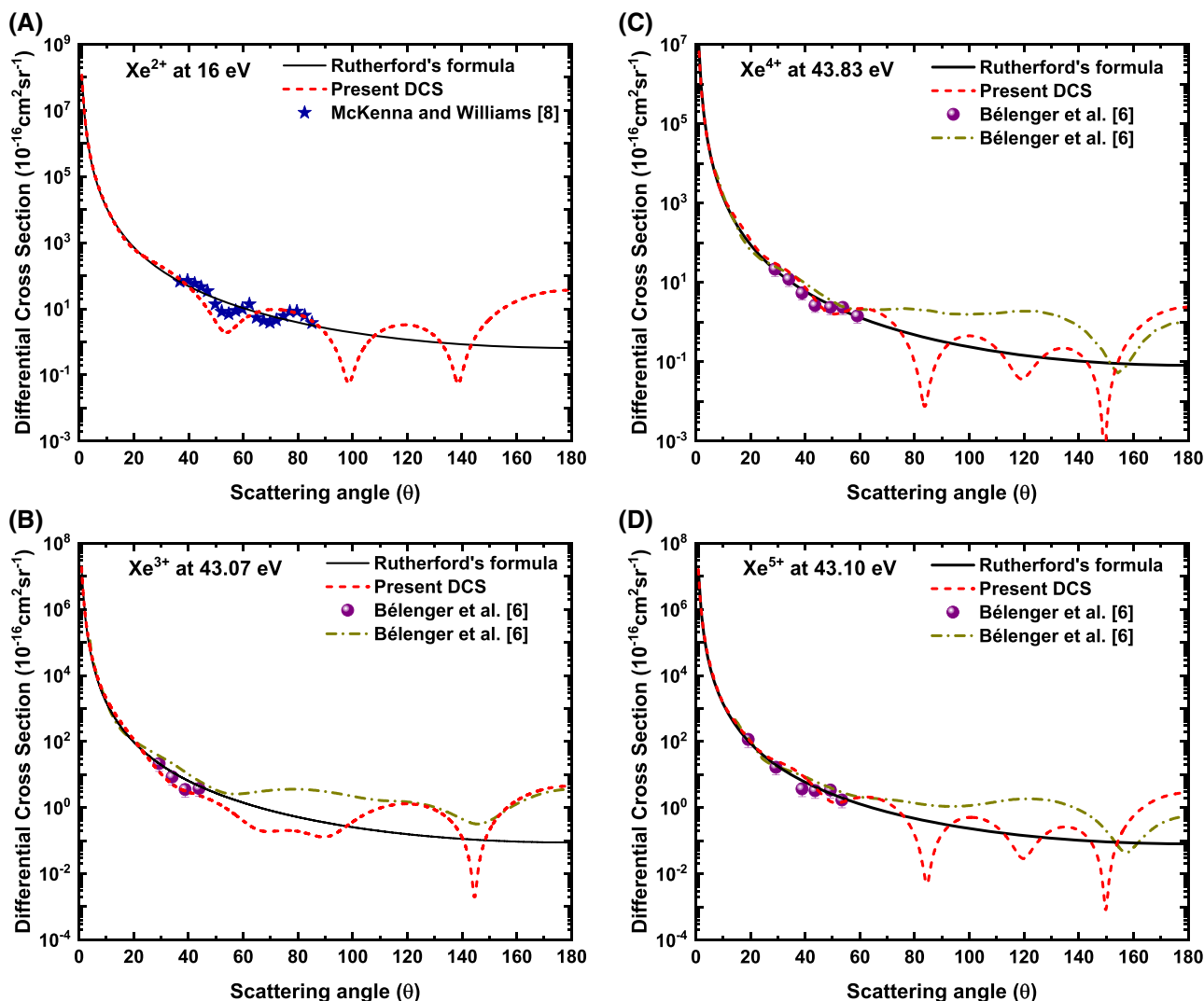


FIGURE 4 Electron impact differential cross sections form (A) Xe^{2+} at 16 eV, (B) Xe^{3+} at 43.07 eV, (C) Xe^{4+} at 43.83 eV, and (D) Xe^{5+} at 43.10 eV

theoretical results of Bélenger et al. [6] and similar features are observed. In the range where experimental results are available up to 60° , all the three results agree completely. Thereafter, the theoretical estimates of Bélenger et al. [6] are slightly higher than ours and without showing any structure in the DCS as seen in our cross section curve. However, one can see a similar minimum in their results around 160° , somewhat closer to the last minima seen in the present calculation. The theoretical results of Bélenger et al. [6] do not show rich structures in their cross section curves may be due to the reason that they did not consider accurate fully relativistic bound xenon ion and projectile electron wave functions in their calculation as we did.

In Figure 5A, the DCS results for Xe^{6+} at 20.69 eV energy have been compared with the measurements (in the angular range 30° – 145°) and calculation of Bélenger et al. [6]. Our cross sections are within the experimental error bars up to scattering angles of 80° . Beyond it, our calculations show slightly lower cross sections and clear structures as compared to the measurements Bélenger et al. [6] while their calculations show usual behavior of slightly overestimating cross sections and not showing any structures. Our DCS results for Xe^{6+} and Xe^{8+} at 50 eV are shown in the Figure 5B,C respectively. These are compared with the measurement and calculation of Huber et al. [3] available in the range of nearly 30° – 75° . In both the figures, the comparison looks similar, that is, our results compare in excellent manner with the theoretical and experimental results of Huber et al. [3] for both the Xe^{6+} and Xe^{8+} ions. For angles beyond 75° , our calculations show more prominent structures while values from Rutherford formula show usual behavior.

We believe, new experiments for larger scattering angles on the ions considered, can provide more meaningful comparison and throw some light on the reliability of our present calculations for all the ions considered in this paper. Due to lack of the experimental results reported at different energies, we have not presented more DCS results at many more incident electron energies as no new physics can come out until the corresponding experimental results are available.

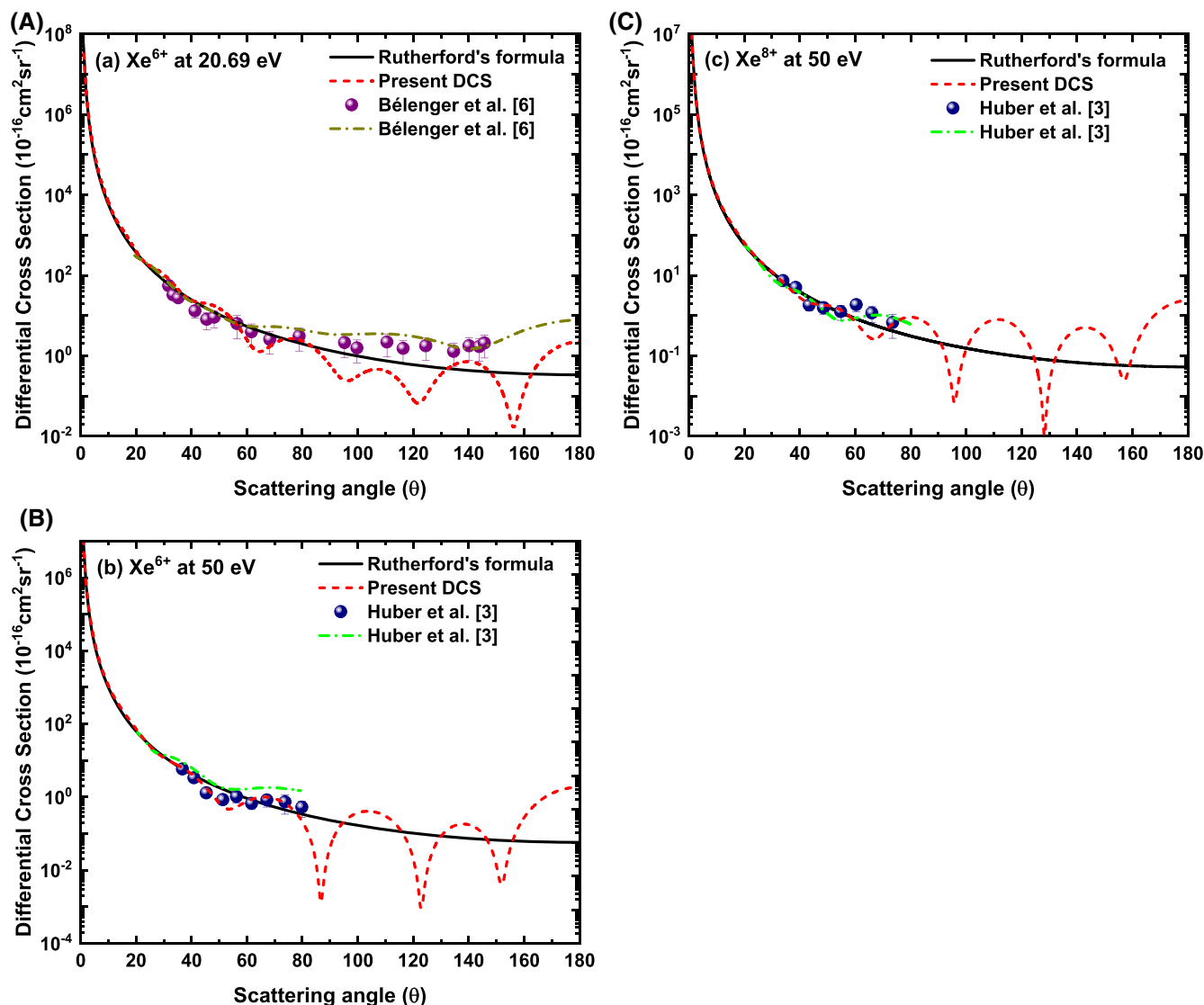


FIGURE 5 Electron impact differential cross sections form (A) Xe⁶⁺ at 20.69 eV, (B) Xe⁶⁺ at 50 eV, and (C) Xe⁸⁺ at 50 eV

4 | CONCLUSIONS

In the present work, we have presented the electron impact DCS for the N^{q+} ($q = 1-3$), Na⁺, Ar^{q+} ($q = 1-3, 7-8$), and Xe^{q+} ($q = 2-6, 8$) ions for the selected incident electron energies where the experimental measurements were performed. This effort was with the view that how close can theory describe the experimental results over and above what Rutherford formula could give us to confirm that for such electron-ion scattering, the Coulomb potential not always fully dominate. To see the effect of short-range potential as atomic ions are having electrons should influence the scattering equally as compared to the Coulomb potential. To explore this, we have used the MCDF framework to describe the ions and projectile electron wave functions were obtained by solving Dirac equations knowingly that for multi-charged ions, especially of inert gases, the spin-orbit and exchange effects will contribute significantly. Further, we have used the complex optical potential in our calculation so that effect of polarization of target ion and inelastic effects through absorption potential are also incorporated in the scattering process. We have noticed that the polarization potential (which is dependent on the accurate ionic polarizability) is an essential component of the potential term that takes care of the accurate minima positions. So, we need more experimental and theoretical calculations to get better and more accurate dipole polarizability of different ions namely for heavier atoms, where the interference behavior or structures seen in the cross sections for the angular distribution are affected by the electron-electron interaction in the ions. Also the in the case of ions having strong Coulomb force which is more dominant for the higher charged state and for that case, the short-range potential might not be that prominent as for the lower charge state. At the end we can say that our results for lower energies show excellent agreement with the experimental results and predict the exact nature of the cross section curves as seen from measurements. Also at the large scattering angles, the influence

of ionic structures shows deviations from the Rutherford cross section results in the DCS. A very few experiments on DCS are available and these only focused in the forward angles and to confirm the correct behavior of DCS structures, thus more experimental work is desirable in the backscattering angles.

ACKNOWLEDGMENTS

The authors, D. M. is thankful to the Ministry of Human Resources and Development (MHRD), Govt. of India, R. S. and L. S. are thankful to SERB-DST, New Delhi, Govt. of India for the sanction of research grants.

AUTHOR CONTRIBUTIONS

Dibyendu Mahato: Formal analysis; investigation; methodology; software; writing-original draft. **Lalita Sharma:** Formal analysis; funding acquisition; methodology; supervision; writing-review and editing. **Rajesh Srivastava:** Assigning the original problem; Formal analysis; funding acquisition; methodology; supervision; writing-review and editing; submitting the paper as corresponding author.

DATA AVAILABILITY STATEMENT

Data available on request from the authors.

ORCID

Rajesh Srivastava  <https://orcid.org/0000-0001-5632-8070>

REFERENCES

- [1] K. Bartschat, M. J. Kushner, *Proc. Natl. Acad. Sci. USA* **2016**, 113, 7026.
- [2] M. Patterson, Ion Propulsion, Facts FS-2004-11-021-GRC **2004**.
- [3] B. A. Huber, C. Ristori, C. Guet, D. K  chler, W. R. Johnson, *Phys. Rev. Lett.* **1994**, 73, 2301.
- [4] B. Srigengan, I. D. Williams, W. R. Newell, *Phys. Rev. A* **1996**, 54, R2540.
- [5] B. Srigengan, P. McKenna, P. McGuinness, I. D. Williams, *Phys. Scr.* **1999**, T80, 272.
- [6] C. B  lenger, P. Defrance, R. Friedlein, C. Guet, D. Jalabert, M. Maurel, C. Ristori, J. C. Rocco, B. A. Huber, *J. Phys. B: At., Mol. Opt. Phys.* **1996**, 29, 4443.
- [7] J. B. Greenwood, I. D. Williams, B. Srigengan, W. R. Newell, J. Geddes, R. W. O'Neill, *Nucl. Instrum. Methods Phys. Res. Sect. B Beam Interact. Mater. Atoms* **1995**, 98, 125.
- [8] P. McKenna, I. D. Williams, *Phys. Scr.* **2001**, T92, 370.
- [9] S. J. Brotton, P. McKenna, G. Gribakin, I. D. Williams, *Phys. Rev. A* **2002**, 66, 062706.
- [10] Z. Wang, J. Matsumoto, H. Tanuma, A. Danjo, M. Yoshino, N. Kobayashi, *J. Phys. B: At., Mol. Opt. Phys.* **2000**, 33, 2629.
- [11] S. Micheau, Z. Chen, A. T. Le, J. Rauschenberger, M. F. Kling, C. D. Lin, *Phys. Rev. Lett.* **2009**, 102, 073001.
- [12] J. T. Shepherd, A. S. Dickinson, *J. Phys. B: At., Mol. Opt. Phys.* **1999**, 32, 513.
- [13] Y. Nishikawa, E. Kimura, T. Kai, Y. Itikawa, S. Nakazaki, *J. Phys. Soc. Jpn.* **2004**, 73, 348.
- [14] M. H. Khandker, A. K. F. Haque, M. Maaza, M. A. Uddin, *Phys. Scr.* **2019**, 94, 075402.
- [15] T. Koga, *Theor. Chim. Acta* **1997**, 95, 113.
- [16] I. P. Grant, *Relativistic Quantum Theory of Atoms and Molecules*, 1st ed., Vol. 40, Springer New York, New York, NY **2007**.
- [17] P. J  nsson, G. Gaigalas, J. Biero  n, C. F. Fischer, I. P. Grant, *Comput. Phys. Commun.* **2013**, 184, 2197.
- [18] J. B. Furness, I. E. McCarthy, *J. Phys. B At. Mol. Phys.* **1973**, 6, 2280.
- [19] F. Salvat, *Phys. Rev. A* **2003**, 68, 012708.
- [20] F. Salvat, A. Jablonski, C. J. Powell, *Comput. Phys. Commun.* **2005**, 165, 157.
- [21] M. P. F. Bristow, *Phys. Fluids* **1972**, 15, 2066.
- [22] P. Meier, R. J. Sandeman, M. Andrews, *J. Phys. B At. Mol. Phys.* **1974**, 7, L339.
- [23] T. Gould, T. Bu  ko, *J. Chem. Theory Comput.* **2016**, 12, 3603.
- [24] J. Mitroy, M. S. Safronova, C. W. Clark, *J. Phys. B: At., Mol. Opt. Phys.* **2010**, 43, 202001.
- [25] R. F. Stewart, B. C. Webster, *J. Chem. Soc., Faraday Trans. 2* **1974**, 70, 524.
- [26] V. P. Shevelko, A. V. Vinogradov, *Phys. Scr.* **1979**, 19, 275.
- [27] C. E. Moore, *Tables of Spectra of Hydrogen, Carbon, Nitrogen, and Oxygen Atoms and Ions*, CRC Press, Boca Raton, FL **1993**.
- [28] J. E. Sansonetti, *J. Phys. Chem. Ref. Data* **2008**, 37, 1659.
- [29] E. B. Saloman, *J. Phys. Chem. Ref. Data* **2010**, 39, 033101.
- [30] E. B. Saloman, *J. Phys. Chem. Ref. Data* **2004**, 33, 765.
- [31] A. E. S. Green, D. L. Sellin, A. S. Zachor, *Phys. Rev.* **1969**, 184, 1.